

Efficient and Probabilistic Adaptive Voxel Mapping for Accurate Online 3D SLAM

Chongjian Yuan^{1,2}, Wei Xu¹, Xiyuan Liu¹, Xiaoping Hong², and Fu Zhang¹,

Abstract—This paper proposes an efficient and probabilistic adaptive voxel mapping method for 3D SLAM. An accurate uncertainty model of point and plane is proposed for probabilistic plane representation. We analyze the need for coarse-to-fine voxel mapping and then use a novel voxel map organized by a Hash table and octrees to build and update the map efficiently. We apply the voxel map to the iterated Kalman filter and construct the maximum posterior probability problem for pose estimation. The experiments on the open KITTI dataset show the high accuracy and efficiency of our method in contrast with other state-of-the-art. Outdoor experiments on unstructured environments with non-repetitive scanning LiDAR further verify the adaptability of our mapping method to different environments and LiDAR scanning patterns.

I. INTRODUCTION

In recent years, with the development of 3D LiDAR technology, especially the emergence of low-cost high-density solid-state LiDARs [1], LiDAR-based simultaneously localization and mapping (SLAM) are implemented in various applications such as autonomous vehicles [2], UAVs (Unmanned Aerial Vehicles) [3], [4] and 3D mobile mapping devices [5], [6]. Most of the modern 3D LiDARs have a large detection range, from tens to hundreds of meters. Although they produce a large number of points, ranging from thousands to millions, of 3D points measurements per second, they all require a certain scanning time to finish a scan. This naturally leads to a sparse to dense point cloud within a scan over time [1]. For multi-line spinning LiDARs, some extra movements are even required due to the fixed scanning location (i.e., elevation angle) of the laser heads. This coarse-to-fine phenomenon is widespread, especially when the LiDAR moves to an un-mapped area (e.g., a quick rotation of a solid-state LiDAR with a small FoV). Moreover, the real-world environments always contain planes of various sizes, such as the different sizes of buildings and roads in urban areas and tree crowns of different sizes in a forest. Therefore the distribution of LiDAR point cloud is very irregular, to be specific, somewhere sparse and somewhere dense, somewhere with large planes, and somewhere with small planar patches.

Due to the irregularity of the LiDAR point cloud mentioned above, the commonly used fix-resolution point-maps in iterated closest point (ICP) [7] and normal distribution

transformation (NDT) [8] based LiDAR SLAM will have difficulty keeping the best performances. The fix-resolution point map will fail to distinguish small planes if the resolution is too large, but if the resolution is too small the computation load will significantly increase. The existing surfel-map based SLAM methods often construct the surfel using the fine-to-coarse methods where valid surfels at the finest level are first extracted and then merged to fewer coarser ones. The fine-to-coarse methods may fail to generate valid finest surfels when the LiDAR point cloud is sparse, such as in the faraway area in the detection range or at the beginning stage when the sensor quickly moved to an un-mapped area.

Another difficulty lies in an efficient and probabilistic representation of 3D maps. The map in LiDAR SLAM is represented in a global frame and it is constructed based on the registered points whose position uncertainty is influenced by the uncertainty of LiDAR pose estimates. For example, the LiDAR rotation estimation uncertainty will introduce a significant uncertainty to faraway points while the influence on nearby ones is much less. Failing to consider these uncertainties may introduce spurious matches and over (or under)-confident constraints during the point registration.

In order to solve the mentioned problems above, we propose a novel voxel mapping method. The contributions are listed as below:

- 1) We propose an adaptive-size and coarse-to-fine voxel construction method, which is robust to the sparsity and irregularity of the LiDAR point cloud. The adaptive voxel map is organized in an octree-hash data structure to increase the efficiency of voxel construction, updates, and inquiries.
- 2) We propose a true Probabilistic voxel map representation, accurately considering the point uncertainty caused by both point measuring and LiDAR pose estimation, to model the uncertainty of planes in the map.
- 3) An implementation of the proposed mapping system in real-world LiDAR odometry and mapping is described and compared with state-of-art methods.

II. RELATED WORKS

Point cloud SLAM has drawn increasing research interests due to recent developments of affordable 3D LiDAR sensors. Recent works on 3D SLAM can be divided into point-map based methods, voxel-based methods and surfel-based methods. ICP is one of the most popular point-map based methods. G-ICP [9] downsamples the point cloud map to a

¹C. Yuan, W. Xu, X. Liu and F. Zhang are with the Department of Mechanical Engineering, The University of Hong Kong, Hong Kong Special Administrative Region, People's Republic of China. {ycj1, xuwei1, xliu1}@connect.hku.hk, fuzhang@hku.hk

²C. Yuan and X. Hong are with the School of System Design and Intelligent Manufacturing, Southern University of Science and Technology, Shenzhen, People's Republic of China. {ycj, hongxp}@sustech.edu.cn

fix-resolution and builds a KD-tree. Then in each iteration of the point cloud registration, several closest points in the map form a plane or edge where the target point is registered to. LOAM [10] introduces feature extraction and separates odometry and mapping to increase efficiency. This framework has been inherited by many recent works [11], [12], [13]. FAST-LIO2 [14] further develops an incremental KD-tree structure to organize the map points, which enables real-time odometry and mapping at a high rate.

Normal distribution transformation (NDT) [15] is a voxel based method where the map consists of many fix-resolution voxels; each voxel is represented by a 3D Gaussian distribution defined by the center position and covariance of points inside it. Compared to the ICP method, NDT does not require nearest neighbor search such that it has improved efficiency, but it requires the voxel to contain enough points to produce an effective and good quality constrain for the point cloud registration. Therefore the NDT's performances are sensitive to the resolution and irregularly of the point cloud.

MRSMap [16] proposes an octree encoded surfel map where the valid surfels can be merged from the finest resolution to coarser resolution (i.e., coarse-to-fine). Inspired by [16], Elasticfusion [17] proposed a commonly used surfel-map representation for RGB-D dense SLAM, where surfel is represented by a center position, normal vector, color, weight, radius, and timestamps. Suma [18] and suma++ [19] propose a LiDAR semantic SLAM framework based on a similar surfel-map as Elasticfusion. Recent works [20], [21] are built on similar fine-to-coarse surfel mapping methods combining the continuous-time trajectory optimization. The fine-to-coarse mapping method works well in dense RGB-D cameras but is sensible to the sparsity and irregularity of the LiDAR point cloud. It also takes much processing time and requires GPU acceleration to achieve real-time performance.

The sensor poses uncertainty is generally considered in most SLAM frameworks such as [22], [23], [24]. Map uncertainty modeling is also important for the consistent and accurate 3D SLAM, but significantly fewer works consider it. The point-map based methods such as ICP and the voxel based methods such as NDT do not consider uncertainty. It should be noted that the points covariance in NDT is only used to represent the voxel in the map, not related to the uncertainty. All the surfel-based methods mentioned above also do not consider the uncertainty of the map. To the authors' knowledge, [25] is the earliest work on a probabilistic model of surfels in a 3D dense map. However, it only considers the measurement uncertainty.

Our proposed method is a voxel-based mapping method for 3d SLAM. Compared to [10], [14], our method does not require the construction of KD-trees, which improves efficiency. Compared to [15], our voxel mapping method is a coarse-to-fine method robust to LiDAR point cloud's irregularity and adaptable to different environments. Compared to [26], [19], our method employs an efficient octree-hash data structure that enables real-time 3D point tracking without GPU acceleration. We also introduce probabilistic plane representation and consider both measurements uncertainty and

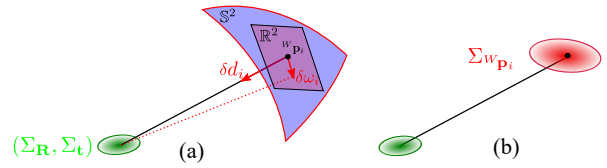


Fig. 1. The uncertainty model of registered point: (a) the LiDAR measurement uncertainty model, including bearing direction and depth measurement uncertainty; (b) point covariance $\Sigma_{w p_i}$ computed from (3).

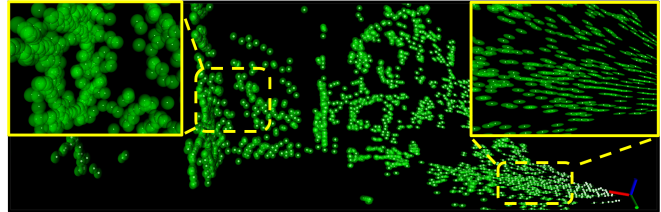


Fig. 2. An example of LiDAR points covariance (green ellipsoid) affected by the uncertainty of LiDAR measurement and pose

associated sensor pose uncertainty while [25] only considers the measurement uncertainty.

III. METHODOLOGY

A. Probabilistic Plane Representation

In this section, the uncertainty model of a plane feature is proposed by considering both uncertainties from the local point measurements and associated sensor pose. Then uncertainty of a plane represented by the normal vector and position is modeled based on the uncertainty of the point.

1) Uncertainty of point ${}^W p_i$:

According to the analysis of the measurement noises for LiDAR sensing in [27], the uncertainty of a LiDAR point in the local LiDAR frame consists of two parts, the ranging uncertainty and the bearing direction uncertainty (see Fig. 1 (a)). Let $\omega_i \in \mathbb{S}^2$ be the measured bearing direction, $\delta\omega_i \sim \mathcal{N}(\mathbf{0}_{2 \times 1}, \Sigma_{\omega_i})$ be the bearing direction noise in the tangent plane of ω_i , d_i be the depth measurement and $\delta d_i \sim \mathcal{N}(0, \Sigma_{d_i})$ be the ranging noise. Then the noise $\delta_{L p_i}$ of the measured point ${}^L p_i$ and its covariance $\Sigma_{L p_i}$ is

$$\delta_{L p_i} = \underbrace{\begin{bmatrix} \omega_i & -d_i[\omega_i]_{\wedge} \mathbf{N}(\omega_i) \end{bmatrix}}_{\mathbf{A}_i} \begin{bmatrix} \delta d_i \end{bmatrix} \sim \mathcal{N}(\mathbf{0}, \Sigma_{L p_i}), \quad (1)$$

$$\Sigma_{L p_i} = \mathbf{A}_i \begin{bmatrix} \Sigma_{d_i} & \mathbf{0}_{1 \times 2} \\ \mathbf{0}_{2 \times 1} & \Sigma_{\omega_i} \end{bmatrix} \mathbf{A}_i^T.$$

where $\mathbf{N}(\omega_i) = [\mathbf{N}_1 \ \mathbf{N}_2] \in \mathbb{R}^{3 \times 2}$ is an orthonormal basis of the tangent plane at ω_i , $[\]_{\wedge}$ denotes the skew-symmetric matrix mapping the cross product. Detailed derivation of equation (1) can be found in [27].

Considering that the LiDAR point ${}^L p_i$ will be further projected to the world frame through the estimated pose ${}^W_L \mathbf{T} = ({}^W_L \mathbf{R}, {}^W_L \mathbf{t}) \in SE(3)$ which has uncertainty $(\Sigma_{\mathbf{R}}, \Sigma_{\mathbf{t}})$ as shown in Fig.1 (b) by the following rigid transformation

$${}^W p_i = {}^W_L \mathbf{R} {}^L p_i + {}^W_L \mathbf{t} \quad (2)$$

Therefore, the uncertainty of the LiDAR point ${}^W p_i$ is hence

$$\Sigma_{w p_i} = {}^W_L \mathbf{R} \Sigma_{L p_i} {}^W_L \mathbf{R}^T + [{}^L p_i]_{\wedge} \Sigma_{\mathbf{R}} [{}^L p_i]_{\wedge}^T + \Sigma_{\mathbf{t}} \quad (3)$$

where $\Sigma_{\mathbf{R}}$ is the uncertainty of the ${}^W_L \mathbf{R}$ in the tangent space and $\Sigma_{\mathbf{t}}$ is the uncertainty of the ${}^W_L \mathbf{t}$. A sample point cloud with covariance is shown in Fig. 2. Considering the

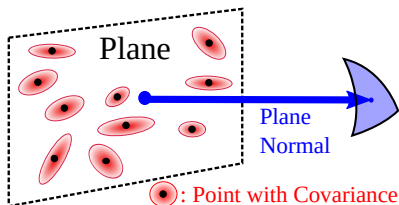


Fig. 3. The Uncertainty model of plane normal.

uncertainty of LiDAR measurement and pose, the covariance of point cloud at different positions has great difference: points at closer distances have their noises dominated by the ranging noise while at further distances dominated by the bearing noise. The uncertainty analysis of a single LiDAR point is also the basis of the uncertainty model of a plane feature.

2) Plane Uncertainty Modelling:

Let a plane feature is made of a group of LiDAR points $W_{\mathbf{p}_i}$ ($i = 1, \dots, N$), each has an uncertainty $W_{\Sigma_{\mathbf{p}_i}}$ due to the measurement noise and pose estimation noise as shown in (3). Denote the points covariance matrix be \mathbf{A} :

$$\bar{\mathbf{p}} = \frac{1}{N} \sum_{i=1}^N W_{\mathbf{p}_i}; \quad \mathbf{A} = \frac{1}{N} (W_{\mathbf{p}_i} - \bar{\mathbf{p}})(W_{\mathbf{p}_i} - \bar{\mathbf{p}})^T; \quad (4)$$

Then, the plane can be represented by its normal vector \mathbf{n} , which is the eigenvector associated with the minimum eigenvalue of \mathbf{A} , and the point $\mathbf{q} = \bar{\mathbf{p}}$, which lies in this plane. As both \mathbf{A} and $\bar{\mathbf{p}}$ are dependent on $W_{\mathbf{p}_i}$, we can denote the plane parameters (\mathbf{n}, \mathbf{q}) as functions of $W_{\mathbf{p}_i}$ shown below:

$$[\mathbf{n}, \mathbf{q}]^T = \mathbf{f}(W_{\mathbf{p}_1}, W_{\mathbf{p}_2}, \dots, W_{\mathbf{p}_N}). \quad (5)$$

Based on the uncertainty analysis in III-A.1, each LiDAR point $W_{\mathbf{p}_i}$ has a noise $\delta_{w_{\mathbf{p}_i}} \sim \mathcal{N}(\mathbf{0}_{3 \times 1}, \Sigma_{w_{\mathbf{p}_i}})$. Therefore, the ground-truth normal vector \mathbf{n}^{gt} and ground-truth position \mathbf{q}^{gt} are

$$\begin{aligned} [\mathbf{n}^{gt}, \mathbf{q}^{gt}]^T &= \mathbf{f}(W_{\mathbf{p}_1} + \delta_{w_{\mathbf{p}_1}}, W_{\mathbf{p}_2} + \delta_{w_{\mathbf{p}_2}}, \dots, W_{\mathbf{p}_N} + \delta_{w_{\mathbf{p}_N}}) \\ &\approx [\mathbf{n}, \mathbf{q}]^T + \sum_{i=1}^N \frac{\partial \mathbf{f}}{\partial W_{\mathbf{p}_i}} \delta_{w_{\mathbf{p}_i}} \end{aligned}$$

Here, $\frac{\partial \mathbf{f}}{\partial W_{\mathbf{p}_i}} = [\frac{\partial \mathbf{n}}{\partial W_{\mathbf{p}_i}}, \frac{\partial \mathbf{q}}{\partial W_{\mathbf{p}_i}}]^T$. Assume \mathbf{A} has the eigenvector matrix \mathbf{U} , the minimum eigenvalue λ_3 and the corresponding eigenvector \mathbf{u}_3 . refer to the [28], we can take the derivative of the \mathbf{n} and \mathbf{q} with respect to each point $W_{\mathbf{p}_i}$ as below:

$$\begin{aligned} \frac{\partial \mathbf{n}}{\partial W_{\mathbf{p}_i}} &= \mathbf{U} \begin{bmatrix} \mathbf{F}_{1,3}^{\mathbf{p}_i} \\ \mathbf{F}_{2,3}^{\mathbf{p}_i} \\ \mathbf{F}_{3,3}^{\mathbf{p}_i} \end{bmatrix}, \quad \mathbf{F}_{m,3}^{\mathbf{p}_i} = \begin{cases} \frac{(W_{\mathbf{p}_i} - \mathbf{q})^T}{N(\lambda_3 - \lambda_m)} (\mathbf{u}_m \mathbf{n}^T + \mathbf{n} \mathbf{u}_m^T), & m \neq 3, \\ \mathbf{0}_{1 \times 3} & m = 3. \end{cases} \\ \frac{\partial \mathbf{q}}{\partial W_{\mathbf{p}_i}} &= \text{diag}(\frac{1}{N}, \frac{1}{N}, \frac{1}{N}) \end{aligned} \quad (6)$$

Then covariance matrix $\Sigma_{\mathbf{n}, \mathbf{q}}$ of \mathbf{n} and \mathbf{q} is:

$$\Sigma_{\mathbf{n}, \mathbf{q}} = \sum_{i=1}^N \frac{\partial \mathbf{f}}{\partial W_{\mathbf{p}_i}} \Sigma_{w_{\mathbf{p}_i}} \frac{\partial \mathbf{f}}{\partial W_{\mathbf{p}_i}}^T \quad (7)$$

It is seen that \mathbf{n} and \mathbf{q} are not independent as they are calculated from the same set of noisy points.

B. Coarse-to-fine and Efficient Voxel Map Construction

In this section, we first explain the motivation for a coarse-to-fine voxel-based map and then the methodology to build

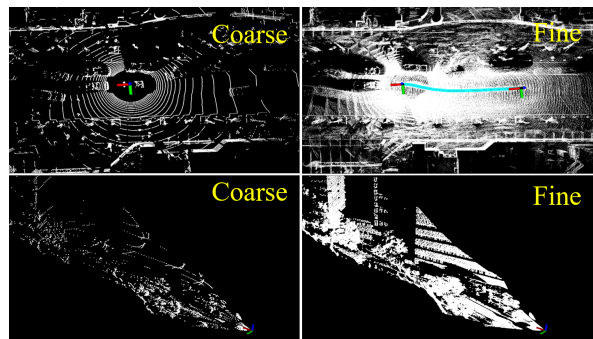


Fig. 4. The coarse-to-fine phenomena in spinning LiDAR (top two figures) and non-repetitive solid-state LiDAR (bottom two figures).

and update the voxel map efficiently.

1) Motivation:

As shown in Fig. 4, LiDAR points are typically sampled sequentially, hence a frame of the point cloud is always accumulated from sparse to dense, especially in outdoor environments where the points are distributed in a larger space. When the point cloud is relatively sparse, common surfel-based fine-to-coarse mapping methods can usually obtain a very small number of planes only, limiting their applications for high-resolutions LiDARs and relatively low frame rate (e.g., 10Hz) to accumulate a sufficient number of points. To address this issue, we propose a coarse-to-fine voxel mapping method that can build a rough voxel map when the point cloud is sparse, and refine the map when more points are received.

2) Voxel Map Construction :

To achieve voxel map construction from coarse-to-fine, we build an adaptive voxel map organized by a Hash table and an octree for each Hash entry (see Algorithm 1). More specifically, we first cut the space (in the global world frame) into voxels, each with the size of the coarse map resolution. Then, for the first LiDAR frame, which defines the world frame, the contained points are distributed into voxels. Voxels populated with points are indexed into a Hash table (Line 1 ~ Line 7). Then, for each populated voxel (Line 8), if all the contained points lie on a plane (the minimum eigenvalue of the point covariance matrix is less than a specified threshold), we will store the plane points and calculate the plane parameters (\mathbf{n}, \mathbf{q}) as in (5) and their uncertainty $\Sigma_{\mathbf{n}, \mathbf{q}}$ as in (7) (Line 9 ~ Line 15); otherwise, the current voxel will break into eight octants and repeat plane checking and voxel cutting in each one until reaching the maximum number of layers (Line 17 ~ Line 18). More detailed processes can be seen in Algorithm 1. As can be seen, the voxel map has voxels of different sizes, each voxel contains a plane feature formed by the LiDAR raw points.

3) Map Update:

For online SLAM, new frames of LiDAR point cloud are continuously coming. A new frame is used to estimate the state of the frame (Section III-D), then the estimated state is used to register the new points into the global map: when the new points lie in an unpopulated voxel, it will construct the voxel (see Algorithm 1). Otherwise, when the

Algorithm 1: Coarse-to-fine voxel map construction

Input : LiDAR point cloud \mathbf{P}_c ;
Maximum voxel size V_{max} ;
Maximum Octree layer L_{max} ;
Plane judgment threshold σ ;

Output: Planar set π_i ($i = 1, 2, \dots, n$)

- 1 **for** each point ${}^W\mathbf{p}_i$ in \mathbf{P}_c **do**
- 2 **if** $\text{HashKey}({}^W\mathbf{p}_i, V_{max}) = \text{Success}$ **then**
- 3 Append ${}^W\mathbf{p}_i$ to the Hash entry.
- 4 **else**
- 5 Create a new Hash entry and assign ${}^W\mathbf{p}_i$ to it.
- 6 **end**
- 7 **end**
- 8 **for** each entry in the Hash table **do**
- 9 Initialize an octree \mathbf{T}_c and initialize the root node with points $\{{}^W\mathbf{p}_i\}$ contained in the Hash entry.
- 10 Set the current layer $L_c = 1$.
- 11 **for** each node of the L_c -th layer of \mathbf{T}_c **do**
- 12 Obtain its contained points $\{{}^W\mathbf{p}_i\}$.
- 13 Calculate the minimum eigenvalue λ_3 of \mathbf{A} as in (4).
- 14 **if** $\lambda_3 < \sigma$ **then**
- 15 Calculate the planar parameter \mathbf{n}, \mathbf{q} and its covariance $\Sigma_{\mathbf{n}, \mathbf{q}}$ as in (5) (7) and save them into the node (i.e., a voxel).
- 16 **else if** current layer $L_c < L_{max}$ **then**
- 17 Distribute the points $\{{}^W\mathbf{p}_i\}$ into the 8 children octants.
- 18 Repeat step 11 ~ 23 for each children octant with $L_c = L_c + 1$.
- 19 **end**
- 20 **else**
- 21 Return.
- 22 **end**
- 23 **end**
- 24 **end**

new points are added to an existing voxel, the parameters and the uncertainty of the plane in the voxel should be updated. This will cause an increased processing time when registering more new points. To address this issue, we find that when the measurement noise of the points is within a certain range, the uncertainty of the plane parameters will quickly converge. Fig. 5 shows the convergence trend of the normal vector uncertainty with the number of points. The position of each point carries a Gaussian noise with a zero mean and a variance of $0.1m^2$. It is seen that the uncertainty of the normal vector converges when the number of points reaches 50. After the uncertainty converges, we discard all historical points and retain the estimated plane parameters (\mathbf{n}, \mathbf{q}) and covariance $\Sigma_{\mathbf{n}, \mathbf{q}}$. Once more new points are coming, we keep only the latest 10 points and calculate the new plane normal vector composed of those 10 points. If the new normal vector and the previously converged normal vector continue to appear relatively large difference, we can assume that this area of the map has changed and needs to

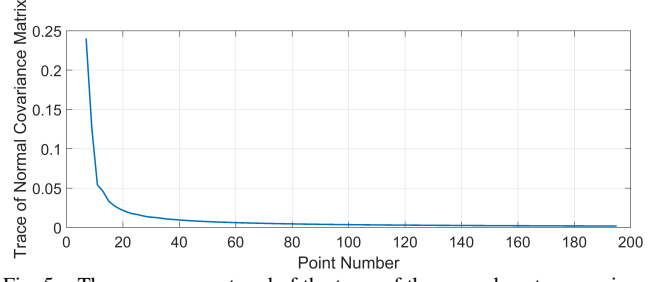


Fig. 5. The convergence trend of the trace of the normal vector covariance matrix with the increase of the number of points

be reconstructed as Algorithm 1.

C. Point-to-plane Match

This section will describe how to match points in a new LiDAR scan with the voxel map, to construct the constrain for the pose estimation and subsequent point cloud registration. Based on the accurate uncertainty modeling of the points and planes, we could easily implement the point-to-plane scan match.

Given a LiDAR point ${}^W\mathbf{p}_i$ predicted in the world frame with the pose prior, we first find which root voxel (with the coarse map resolution) it lies in by its Hash key. Then, all the contained sub-voxels are polled for a possible match with the point. Specifically, let a sub-voxel contains a plane with normal \mathbf{n}_i and center \mathbf{q}_i , we calculate the point-to-plane distance:

$$d_i = \mathbf{n}_i^T ({}^W\mathbf{p}_i - \mathbf{q}_i) \quad (8)$$

As analyzed above, the normal vector \mathbf{n}_i , the LiDAR point ${}^W\mathbf{p}_i$, and the center \mathbf{q}_i have uncertainties. Consider the uncertainty of all the variables, we obtain:

$$\begin{aligned} d_i &= (\mathbf{n}_i^{gt} \boxplus \delta_{\mathbf{n}_i})^T [({}^W\mathbf{p}_i^{gt} + \delta_{w_{\mathbf{p}_i}}) - \mathbf{q}_i^{gt} - \delta_{\mathbf{q}_i}] \\ &\approx \underbrace{\mathbf{n}_i^{gt T} ({}^W\mathbf{p}_i^{gt} - \mathbf{q}_i^{gt})}_0 + \underbrace{\mathbf{J}_{\mathbf{n}_i} \delta_{\mathbf{n}_i} + \mathbf{J}_{\mathbf{q}_i} \delta_{\mathbf{q}_i} + \mathbf{J}_{w_{\mathbf{p}_i}} \delta_{w_{\mathbf{p}_i}}}_{\mathbf{w}_i} \end{aligned}$$

which implies

$$d_i \sim \mathcal{N}(0, \Sigma_{\mathbf{w}_i}), \quad \Sigma_{\mathbf{w}_i} = \mathbf{J}_{\mathbf{w}_i} \Sigma_{\mathbf{n}_i, \mathbf{q}_i, w_{\mathbf{p}_i}} \mathbf{J}_{\mathbf{w}_i}^T, \quad (9)$$

where,

$$\begin{aligned} \mathbf{J}_{\mathbf{w}_i} &= [\mathbf{J}_{\mathbf{n}_i}, \mathbf{J}_{\mathbf{q}_i}, \mathbf{J}_{w_{\mathbf{p}_i}}] = [({}^W\mathbf{p}_i - \mathbf{q}_i)^T, -\mathbf{n}_i^T, \mathbf{n}_i^T] \\ \Sigma_{\mathbf{n}_i, \mathbf{q}_i, w_{\mathbf{p}_i}} &= \begin{bmatrix} \Sigma_{\mathbf{n}_i, \mathbf{q}_i} & 0 \\ 0 & \Sigma_{w_{\mathbf{p}_i}} \end{bmatrix}. \end{aligned} \quad (10)$$

That is being said, if the point lies on the candidate plane, its distance d_i should be subject to the distribution in (9). Therefore, we can judge whether the measured distance from a point to a plane falls within 3σ , if so, it is selected to be an effective match. Besides, if a point matches more than one plane based on the 3σ criterion, the plane with the highest probability will be matched. If no plane passes the 3σ test, the point is discarded to remove the possible false matches caused by voxel quantization.

D. State Estimation

We build a LiDAR odometry system based on an iterated Kalman filter similar to FAST-LIO [3]. Let us assume that we are given a state estimation prior $\hat{\mathbf{x}}_k$ with covariance $\hat{\mathbf{P}}_k$ (e.g., from a constant velocity assumption or IMU propagation, e.g., [3]). This prior will be fused with the point-to-plane

distance matched in Section III-C to form a maximum posterior probability (MAP) estimation. Specifically, the i -th valid point-to-plane match leads to the observation equation

$$\mathbf{z}_i = \mathbf{h}_i(\mathbf{x}_k) + \mathbf{v}_i \quad (11)$$

where \mathbf{z}_i is the point-to-plane distance residual d_i in equation (8), $\mathbf{h}_i(\mathbf{x}_k)$ is the observation function and $\mathbf{v}_i \sim (0, \mathbf{R}_i)$ is the observation noise. By substituting the state \mathbf{x}_k (i.e., the sensor pose \mathbf{T}_k) into (8) and linearize it around the current state update $\bar{\mathbf{x}}_k$, we obtain:

$$\begin{aligned} \mathbf{z}_i &= \mathbf{h}_i(\mathbf{x}_k) + \mathbf{v}_i = \mathbf{n}_i^T ({}^W\mathbf{p}_i - \mathbf{q}_i) \\ &= (\mathbf{n}_i^{gt} \boxplus \delta_{\mathbf{n}_i})^T [(\mathbf{T}_k^{gt} \boxplus \delta_{\mathbf{T}_k}) ({}^L\mathbf{p}_i^{gt} + \delta_{L\mathbf{p}_i}) - \mathbf{q}_i^{gt} - \delta_{\mathbf{q}_i}] \\ &\approx \underbrace{\mathbf{n}_i^{gtT} (\mathbf{T}_k^{gtL} \mathbf{p}_i^{gt} - \mathbf{q}_i^{gt})}_0 + \underbrace{\mathbf{J}_{\mathbf{T}_i} \delta_{\mathbf{T}_k}}_{\mathbf{H}_i \delta \mathbf{x}_k} + \underbrace{\mathbf{J}_{\mathbf{n}_i} \delta_{\mathbf{n}_i} + \mathbf{J}_{\mathbf{q}_i} \delta_{\mathbf{q}_i} + \mathbf{J}_{L\mathbf{p}_i} \delta_{L\mathbf{p}_i}}_{\mathbf{v}_i} \end{aligned}$$

which implies

$$\mathbf{R}_i = \mathbf{J}_{\mathbf{v}_i} \Sigma_{\mathbf{n}_i, \mathbf{q}_i, L\mathbf{p}_i} \mathbf{J}_{\mathbf{v}_i}^T, \quad (12)$$

where

$$\begin{aligned} \mathbf{J}_{\mathbf{v}_i} &= [\mathbf{J}_{\mathbf{n}_i}, \mathbf{J}_{\mathbf{q}_i}, \mathbf{J}_{L\mathbf{p}_i}] = [(\bar{\mathbf{T}}_k^L \mathbf{p}_i - \mathbf{q}_i)^T, -\mathbf{n}_i^T, \mathbf{n}_i^T \bar{\mathbf{R}}_k] \\ \Sigma_{\mathbf{n}_i, \mathbf{q}_i, L\mathbf{p}_i} &= \begin{bmatrix} \Sigma_{\mathbf{n}_i, \mathbf{q}_i} & 0 \\ 0 & \Sigma_{L\mathbf{p}_i} \end{bmatrix}. \end{aligned}$$

Finally, combining the state prior with all effective measurements, we can obtain the MAP estimation:

$$\min_{\mathbf{x}_k} \left(\|\mathbf{x}_k \boxminus \bar{\mathbf{x}}_k\|_{\bar{\mathbf{P}}_k}^2 + \sum_{i=1}^m \|d_i - \mathbf{H}_i \cdot (\mathbf{x}_k \boxminus \bar{\mathbf{x}}_k)\|_{\mathbf{R}_i}^2 \right) \quad (13)$$

where the first part is the state prior and the second part is the measurement observation.

IV. EXPERIMENT

A. Comparison on open KITTI dataset

We evaluate our approach on the odometry datasets of the KITTI Vision Benchmark [2], where the LiDAR data is collected by Velodyne HDL-64E S2 at a rate of 10 Hz. All the experiments are conducted on a desktop computer with Intel i7-10700 @ 2.9 GHz with 16 GB RAM and Nvidia GeForce GTX 730 with 2 GB RAM.

Comparison with state-of-the-art. We compare our method with FAST-LIO2 [14], an ICP-based LiDAR odometry approach. Suma [26], a surfel-based LiDAR SLAM approach, and Lego-Loam [11]. We run our algorithm on all sequences with the same parameters. For Suma and LeGO-Loam, we conducted the experiments using their own implementation with the default parameters. For Fast-Lio2, the point clouds in KITTI dataset are undistorted already, therefore we use a constant velocity model to serve as the motion prior required by FAST-LIO2 as well as our method (see (13)).

We use absolute translational error (RMSE) to evaluate the accuracy of the odometer. All the trajectories are registered by ICP through the first 20% part, then the RMSE after registration is calculated and the final result is recorded in Table I. As can be seen, we do better than the other algorithms except for sequences 03 and 04, especially in long-term sequences like 00, 02 and 08. To further show the high accuracy of our method, we plot the trajectories

of all sequences in Fig. 6. It is seen that all of our global trajectories are very close to the ground truth, which verify the high accuracy of our method.

Runtime evaluation. We calculate the average processing time and the corresponding standard deviation for all sequences, summarized in Table I. Suma uses GPU to accelerate, while other methods only use CPU. Suma takes more time in our experiment than the original paper [26] due to the difference in GPU performance. As can be seen, our method has the lowest processing time, and the next is FAST-LIO2 [14]. When compared to FAST-LIO2 [14] and Lego-LOAM [11], we use the voxel map described in III-B.2 to avoid building a KD-tree in real-time [14] or periodically [11]. Moreover, searching neighbor points on KD-trees has a time complexity $\log(n)$, where n is the number of points in the dense point cloud map. In contrast, the speed of searching the adjacent plane in the voxel map is near to $O(1)$, which ensures efficiency. Fig. 7 shows the detailed processing time needed to process sequence 00 from the KITTI Odometry dataset. The average processing time is only 24.2ms and the maximum processing time is 44.2ms. The major time-consuming part is the scan matching process as we calculate and use the covariance information of each LiDAR point.

B. Unstructured Environment Test

In order to show the adaptability of our mapping method to different environments and LiDAR scanning patterns, we test it in unstructured environments using a solid-state LiDAR Livox Avia. Moreover, we use the built-in IMU of the LiDAR sensor to compensate the motion distortion and provide motion prior similar to FAST-LIO2 [14].

1) *Park Environment:* In this experiment, we used a handheld device to collect the LiDAR and IMU data in a large park filled with trees. In order to show the drift, the data collection route starts and ends at the same place. Besides, to avoid randomness, we collect the data of three different trajectories, of which two groups are 400m long around the periphery of the park, and one group is 800m long around the periphery and the interior of the park. The mapping result of the park with the longest trajectory is shown in Fig. 8(a). The drift of the three groups of data are respectively 0.05m, 0.04m and 0.08m, which indicates that our method is extremely low drift. The scan rate is set to 10 Hz in this experiment, and the average processing time of a scan is 10 ms with an average of 1546 effective matching points.

It is noted from the Fig. 8(a) that the park is filled with a large number of trees and has few structures (see the aligned satellite image in Fig. 8(a)) similar to those found in the urban environment. However, due to our adaptive coarse-to-fine voxel map, we can make good use of information from the tree trunks and some other small structural planes. As we set the coarse map resolution in this scene to 2m and the deepest layer of the octree to 3, we finally obtained many planes of three sizes: 2928 planes with the size of 2m, 26069 planes with the size of 1m, and 104352 planes with the size of 0.5m. An example of a plane map can be seen in Fig. 8(b).

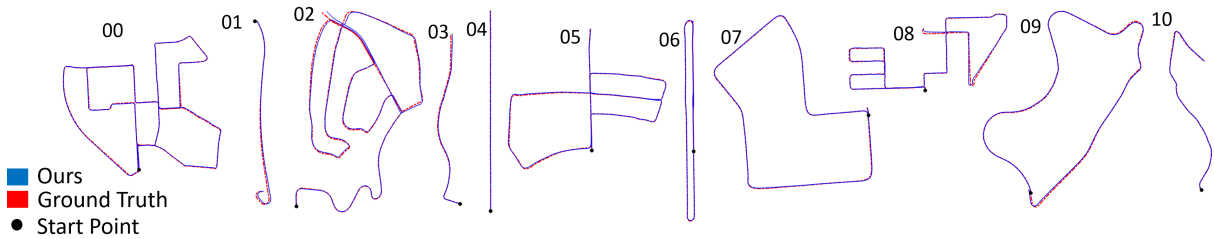


Fig. 6. Trajectories of sequence 00 to 10. The blue trajectories are our odometry output and the red trajectories are the ground truth. The black dot represents the starting point.

Approach	00	01	02	03	04	05	06	07	08	09	10	mean (ms)	std (ms)
Ours	3.91	59.76	20.39	7.54	1.92	2.59	3.08	2.55	5.64	6.72	5.46	26.45	9.87
Suma [26]	5.82	105.49	88.37	9.26	1.55	3.12	3.47	2.66	14.33	12.11	7.52	129.36	62.22
FAST-LIO2 [14]	4.92	104.94	29.93	7.35	2.76	3.04	3.41	3.11	9.19	13.02	12.47	29.11	10.94
Lego-loam [11]	11.32	498.30	80.88	5.37	2.66	2.86	3.56	3.03	6.96	16.60	11.46	57.13	21.52

TABLE I
RESULT(RMSE IN METERS) ON KITTI ODOMETRY(TRAINING)

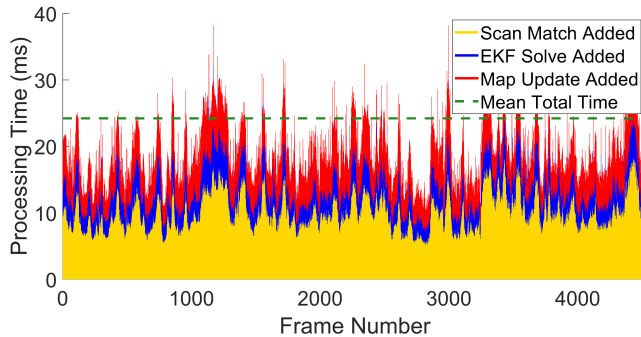


Fig. 7. Processing time needed to process sequence 00.

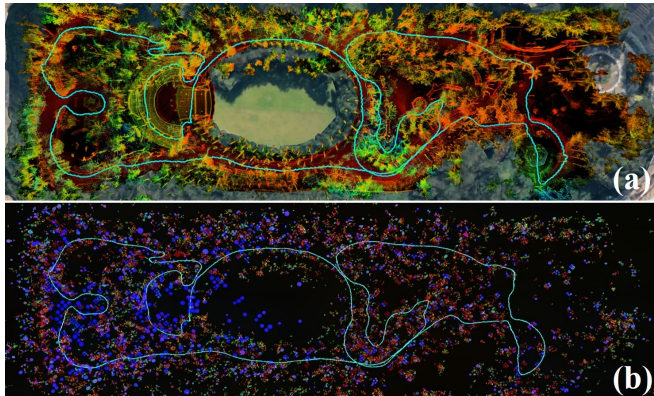


Fig. 8. (a) The point cloud map is aligned with the satellite image. (b) The plane map constructed in the park environment

2) *Mountain Environment*: In this experiment, we use a UAV to carry our LiDAR and face the LiDAR to the ground to collect point cloud data on a mountain. Compared to the park, the mountain environment is even less structured and more challenging. The mapping results of the mountain are shown in Fig. 9(a) and the details of some locally enlarged views are shown in Fig. 9(b) and the start point and end point are shown in Fig. 9(c). The average flight altitude is around 80m. The total length of the trajectory is 3500m and the final drift is 6.7m. The scan rate is set to 10 Hz in this experiment, and the average processing time of a scan is 50 ms with an average of 7630 effective matching points.

V. CONCLUSION

This paper proposes an efficient, probabilistic adaptive voxel mapping method for online 3D SLAM. An accurate un-

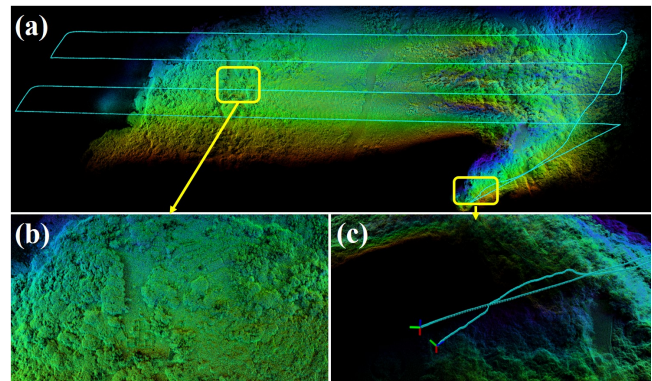


Fig. 9. (a) The mapping result of a mountain. (b) Some details of the mapping results. (c) The start point and end point of the trajectory.

certainly model of the LiDAR point and plane is proposed by considering both measurements uncertainty and associated sensor pose uncertainty. The voxel map is constructed using coarse-to-fine adaptive resolution method, which is robust to different LiDAR scanning patterns and environments. This paper also shows how to implement the proposed mapping method in the iterated Kalman filter based LiDAR SLAM. The tests in the KITTI dataset show that our method can achieve better performance than both ICP-based method and surfel-based method. The proposed voxel mapping method not only performs well in the spinning LiDAR in structured urban environments, but also shows good performance with non-repetitive small FoV LiDAR in unstructured environments such as parks and mountains.

ACKNOWLEDGMENT

This project is supported by DJI under the grant 200009538 and in part by SUSTech startup fund (Y01966105). The authors gratefully acknowledge Livox Technology for the equipment support during the whole work. The authors would like to thank Ambit-Geospatial for the helps in the outdoor aerial experiment.

REFERENCES

- [1] Z. Liu, F. Zhang, and X. Hong, "Low-cost retina-like robotic lidars based on incommensurable scanning," *IEEE/ASME Transactions on Mechatronics*, pp. 1–1, 2021.

- [2] A. Geiger, P. Lenz, and R. Urtasun, "Are we ready for autonomous driving? the kitti vision benchmark suite," in *2012 IEEE conference on computer vision and pattern recognition*. IEEE, 2012, pp. 3354–3361.
- [3] W. Xu and F. Zhang, "Fast-lio: A fast, robust lidar-inertial odometry package by tightly-coupled iterated kalman filter," *IEEE Robotics and Automation Letters*, pp. 1–1, 2021.
- [4] Y. Okubo, C. Ye, and J. Borenstein, "Characterization of the hokuyo urg-04lx laser rangefinder for mobile robot obstacle negotiation," in *Unmanned Systems Technology XI*, vol. 7332. International Society for Optics and Photonics, 2009, p. 733212.
- [5] J. Zhang and S. Singh, "Visual-lidar odometry and mapping: Low-drift, robust, and fast," in *2015 IEEE International Conference on Robotics and Automation (ICRA)*. IEEE, 2015, pp. 2174–2181.
- [6] R. Ravi, A. Habib, and D. Bullock, "Pothole mapping and patching quantity estimates using lidar-based mobile mapping systems," *Transportation Research Record*, vol. 2674, no. 9, pp. 124–134, 2020.
- [7] G. C. Sharp, S. W. Lee, and D. K. Wehe, "Icp registration using invariant features," *IEEE Transactions on Pattern Analysis and Machine Intelligence*, vol. 24, no. 1, pp. 90–102, 2002.
- [8] P. Biber and W. Straßer, "The normal distributions transform: A new approach to laser scan matching," in *Proceedings 2003 IEEE/RSJ International Conference on Intelligent Robots and Systems (IROS 2003)(Cat. No. 03CH37453)*, vol. 3. IEEE, 2003, pp. 2743–2748.
- [9] A. Segal, D. Haehnel, and S. Thrun, "Generalized-icp," in *Robotics: science and systems*, vol. 2, no. 4. Seattle, WA, 2009, p. 435.
- [10] J. Zhang and S. Singh, "Loam: Lidar odometry and mapping in real-time," in *Robotics: Science and Systems*, vol. 2, no. 9, 2014.
- [11] T. Shan and B. Englot, "Lego-loam: Lightweight and ground-optimized lidar odometry and mapping on variable terrain," in *2018 IEEE/RSJ International Conference on Intelligent Robots and Systems (IROS)*. IEEE, 2018, pp. 4758–4765.
- [12] J. Lin and F. Zhang, "Loam livox: A fast, robust, high-precision lidar odometry and mapping package for lidars of small fov," in *2020 IEEE International Conference on Robotics and Automation (ICRA)*. IEEE, 2020, pp. 3126–3131.
- [13] H. Ye, Y. Chen, and M. Liu, "Tightly coupled 3d lidar inertial odometry and mapping," in *2019 International Conference on Robotics and Automation (ICRA)*. IEEE, 2019, pp. 3144–3150.
- [14] W. Xu, Y. Cai, D. He, J. Lin, and F. Zhang, "Fast-lio2: Fast direct lidar-inertial odometry," 2021.
- [15] M. Magnusson, A. Lilienthal, and T. Duckett, "Scan registration for autonomous mining vehicles using 3d-ndt," *Journal of Field Robotics*, vol. 24, no. 10, pp. 803–827, 2007.
- [16] J. Stückler and S. Behnke, "Multi-resolution surfel maps for efficient dense 3d modeling and tracking," *Journal of Visual Communication and Image Representation*, vol. 25, no. 1, pp. 137–147, 2014.
- [17] T. Whelan, R. F. Salas-Moreno, B. Glocker, A. J. Davison, and S. Leutenegger, "Elasticfusion: Real-time dense slam and light source estimation," *The International Journal of Robotics Research*, vol. 35, no. 14, pp. 1697–1716, 2016.
- [18] J. Behley and C. Stachniss, "Efficient surfel-based slam using 3d laser range data in urban environments," in *Robotics: Science and Systems*, vol. 2018, 2018.
- [19] X. Chen, A. Milioto, E. Palazzolo, P. Giguere, J. Behley, and C. Stachniss, "Suma++: Efficient lidar-based semantic slam," in *2019 IEEE/RSJ International Conference on Intelligent Robots and Systems (IROS)*. IEEE, 2019, pp. 4530–4537.
- [20] D. Droeschel, M. Schwarz, and S. Behnke, "Continuous mapping and localization for autonomous navigation in rough terrain using a 3d laser scanner," *Robotics and Autonomous Systems*, vol. 88, pp. 104–115, 2017.
- [21] J. Quenzel and S. Behnke, "Real-time multi-adaptive-resolution-surfel 6d lidar odometry using continuous-time trajectory optimization," *arXiv preprint arXiv:2105.02010*, 2021.
- [22] C. Forster, L. Carlone, F. Dellaert, and D. Scaramuzza, "On-manifold preintegration for real-time visual-inertial odometry," *IEEE Transactions on Robotics*, vol. 33, no. 1, pp. 1–21, 2016.
- [23] T. Qin, P. Li, and S. Shen, "Vins-mono: A robust and versatile monocular visual-inertial state estimator," *IEEE Transactions on Robotics*, vol. 34, no. 4, pp. 1004–1020, 2018.
- [24] A. I. Mourikis and S. I. Roumeliotis, "A multi-state constraint kalman filter for vision-aided inertial navigation," in *Proceedings 2007 IEEE International Conference on Robotics and Automation*. IEEE, 2007, pp. 3565–3572.
- [25] C. Park, S. Kim, P. Moghadam, C. Fookes, and S. Sridharan, "Probabilistic surfel fusion for dense lidar mapping," in *Proceedings of the IEEE International Conference on Computer Vision Workshops*, 2017, pp. 2418–2426.
- [26] J. Behley and C. Stachniss, "Efficient surfel-based slam using 3d laser range data in urban environments," in *Proc. of Robotics: Science and Systems (RSS)*, 2018.
- [27] C. Yuan, X. Liu, X. Hong, and F. Zhang, "Pixel-level extrinsic self calibration of high resolution lidar and camera in targetless environments," *IEEE Robotics and Automation Letters*, vol. 6, no. 4, pp. 7517–7524, 2021.
- [28] Z. Liu and F. Zhang, "Balm: Bundle adjustment for lidar mapping," *IEEE Robotics and Automation Letters*, vol. 6, no. 2, pp. 3184–3191, 2021.